ARTICLE

A modified constitutive model based on Arrhenius-type equation to predict the flow behavior of Fe–36%Ni Invar alloy

Shuai He and Chang-sheng Li[a)]
State Key Laboratory of Rolling and Automation, Northeastern University, Shenyang 110819, China

Zhen-yi Huang
School of Metallurgic Engineering, Anhui University of Technology, Ma'Anshan 243000, China

Jian-jun Zheng
State Key Laboratory of Rolling and Automation, Northeastern University, Shenyang 110819, China

The predictability of modified constitutive model, based on Arrhenius type equation, for illustrating the flow behavior of Fe–36%Ni Invar alloy was investigated via isothermal hot compression tests. The hot deformation tests were carried out in a temperature range of 850–1100 °C and strain rates from 0.01 to 10 s^{-1}. True stress-true strain curves exhibited the dependence of the flow stress on deformation temperatures and strain rates, which then described in Arrhenius-type equation by Zener–Holloman parameter. Moreover, the related material constants and hot deformation activation energy (Q) in the constitutive model were calculated by considering the effect of strain as independent function on them and employing sixth polynomial fitting. Subsequently, the performance of the modified constitutive equation was verified by correlation coefficient and average absolute relative error which were estimated in accordance with experimental and predicted data. The results showed that the modified constitutive equation possess reliable and stable ability to predict the hot flow behavior of studied material under different deformation conditions. Meanwhile, Zener–Holloman parameter map was established according to the modified constitutive equation and used to estimate the extent of dynamic recrystallization.

I. INTRODUCTION

It is well known that the hot deformation processes (forging, rolling, and extruding et al.) of metals and alloys are extremely complex and regarded as a crucial part in the industrial production.[1–3] In this context, a considerable amount of research has been devoted to acquire the accurate predictability of the material models to simulate the deformation process. Moreover, the modeling of hot deformation behavior is generally established through the constitutive equations. Accordingly, a number of constitutive models have occurred through hot compressive or tensile experiments to clarify the relationship between the flow stress and deformation parameters (i.e., temperatures and strain rates) for different metals and alloys so as to better guide the hot working process.[4–7]

According to recent research, Samantaray et al.[8] carried out a study to compare the predictability of Johnson–Cook (JC), modified Zerilli–Armstrong (ZA) and strain-compensated Arrhenius-type constitutive models for the flow behavior of 9Cr–1Mo steel, and eventually found that Arrhenius-type constitutive models revealed a higher prediction accuracy than the other models in the hot working domain. Abbasi-Bani et al.[9] introduced two phenomenological constitutive equations (Johnson Cook and Arrhenius-type ones) to depict the high temperature flow behavior of Mg–6Al–1Zn alloy during hot compression tests, and also concluded that the Arrhenius-type equations were more reliable for the material deformation process. Same as above, the investigations of the flow behavior of Al–0.62Mg–0.73Si aluminum alloy[10] and ferritic stainless steel[11] still proved the prediction capability of the Arrhenius-type model was stronger than the Johnson–Cook model. Furthermore, a modified Arrhenius-type constitutive equation considering the effect of strain on material constant was developed under hot deformation conditions to describe the flow stress of different materials, such as Ti–20Zr–6.5Al–4V alloy,[12] aluminum alloy (AA2030 alloy,[13] Al–Zn–Mg–Cu alloy,[14] and AA6N01 alloy[15]), magnesium alloy (AZ81 alloy,[16] AZ31B alloy,[17] and Mg–4Li–1Al alloy[18]), 17%Cr ferritic stainless steel,[19] AISI 420 stainless steel,[20] Fe–21Mn–2.5Si–1.5Al steel,[21] Nb–Ti micro alloyed steel,[22] and Nickel-based corrosion-resistant alloy

(N08028).[23] Additionally, based on modified Zerilli–Armstrong model, a thermo-viscoplastic constitutive model was proposed by Samantaray et al.[24] and used to successfully describe the flow behavior of IFAC-1 austenitic stainless steel under the hot working conditions. Nevertheless, a comparison between the modified Zerilli–Armstrong and the Arrhenius-type model about the flow behavior predictability of BFe10-1-2 cupronickel alloy also illustrated that the latter had a better performance.[25] Similarly, Guan et al.[26] compared the predictability of a phenomenological constitutive equation and an empirical constitutive equation to model the flow behavior of Al–Zn–Mg–Zr alloy, and then found the latter had higher accuracy over wide range of strain rates and strains. By taking the temperature softening coefficient and strain rate sensitivity into account, an amended Fields–Backofen (FB) equation was applied to precisely describe the constitutive behavior of magnesium alloy (as-cast AZ31Bb alloy[27] and extruded AZ61 alloy[28]) under hot compression tests. Meanwhile, the artificial neural network (ANN) model with a feedforward back propagation has been evaluated during hot deformation process to predict the flow behavior of different materials, such as as-cast TC21 titanium alloy,[29] Ti600 alloy,[30] ZK60 alloy,[31] AZ81 magnesium alloy,[32] 7050 aluminum alloy,[33] 20MnNiMo low carbon alloy,[34] and Cu–0.4Mg alloy.[35]

On the other hand, researchers investigated the effect of rationalized processing parameters on microstructure evolution or mechanical properties of different metals and alloys, such as as-cast Ti60 titanium alloy,[36] bainitic pipeline steel,[2] TRIP780 steel,[3] 316 L(N) austenitic stainless steel,[37] titanium alloy,[38] aluminum alloy (AA2030 alloy,[13] 7050-H112 alloy,[39] and 7050 alloy[40]) and dual super–alloy.[41] It is worth noting that some typical metallurgical phenomena [dynamic recovery, dynamic recrystallization (DRX), work hardening behavior, grain boundary characteristic distribution] appeared at microstructure evolution during the hot deformation process and DRX can occur especially in face-centered cubic structure alloys with low stacking fault energy.[19] Feng et al.[42] investigated the flow stress of Al–7.68Zn–2.12Mg–1.98Cu–0.12Zr alloy based on the kinetics of DRX and dislocation density theory and then analyzed the microstructure by combining Z–H parameter as well as processing map. Bobbili et al.[43] not only established the DRX kinetic equation of biomedical Ti–13Nb–13Zr alloy under the high temperature compression tests but also found the decrease of strain rate and increase of deformation temperature both promoted the process of DRX. Also, some investigators researched the DRX behavior of different metals and alloys, such as nickel-based super-alloy,[44] 6X82 aluminum alloy,[45] stainless steel (ultra-pure 17%Cr ferritic,[19] AISI 420,[20] 304 H austenitic,[46] and LDX 2101 duplex[47]), AZ31 and ME21

magnesium alloys,[48] and nickel–chromium alloy (800H).[49]

As a face-centered cubic (FCC) special metallic functional material, Fe–36%Ni Invar alloy is widely used in the field of precision instrument and electronic industry, particularly served as liquefied natural gas (LNG) carriers. The main reason is that this alloy has a low thermal expansion coefficient below the Curie point.[50,51] So, the Invar alloys have attracted extensive investigations such as magnetic phase diagram,[52] the hot ductility,[53] mechanical alloying,[54] and the tensile properties.[55,56] Until recently, there is little information available in literature about the hot compressive behavior of Fe–36%Ni Invar alloy. Therefore, the main objective of this work is to investigate the hot deformation behavior of Fe–36%Ni Invar alloy via isothermal hot compression tests at various deformation temperatures and strain rates. To be specific, a modified Arrhenius-type constitutive equation was derived which involved the flow stress, deformation temperature, and strain rate with consideration of the compensation of strain to reveal the flow behavior of experimental material at elevated temperatures.

II. EXPERIMENTAL PROCEDURE

Fe–36%Ni Invar alloy was prepared by vacuum melting and machined into cylindrical specimens with diameter of 10 mm and length of 15 mm for measurements. The chemical composition of the experimental alloy is 0.0033C–0.0287Si–0.022Mn–0.0101P–0.0013S–0.0124Al–0.0069O–0.0021N–36.59Ni–(bal.) Fe.

Hot compression tests were carried out at six different temperatures (850, 900, 950, 1000, 1050, and 1100 °C) as well as four different strain rates (0.01, 0.1, 1, and 10 s^{-1}) by employing MMS-300 thermo–mechanical simulator. The specimens were heated at a rate of 10 °C/s to 1200 °C, held for 180 s to homogenize the microstructure, and then cooled to test temperatures at a cooling rate of 5 °C/s. The specimens were also held for 20 s to eliminate the thermal gradient before the compression tests. The specimens were deformed to a true strain of 0.7 and then immediately water quenched to retain the hot deformation microstructure. The flat ends of the specimens were covered by a lubricant consisting of graphite powder and machine oil so as to reduce the fraction between the specimen and the die during hot compression.

III. RESULTS AND DISCUSSION

A. Flow stress behavior

Flow stress curves of Fe–36%Ni Invar alloy at different temperatures and strain rates are presented in

Fig. 1. It can be clearly observed that the flow stress markedly increases with decrease in deformation temperature and rise in strain rate. Moreover, Fig. 1 typically reflected a work hardening region and subsequently dynamic softening, namely, these two phenomena are main deformation mechanism under experimental conditions. What's more, work hardening is resulted from the increase of dislocation density and interaction of dislocation, while the annihilation and restructuring of dislocation can lead to dynamic softening.[19] Figs. 1(a) and 1(b) noticeably experience a single peak stress followed by a continuous decline toward a steady stress, which exhibits the occurrence of DRX during hot deformation. By contrast, the flow stress curves of Figs. 1(c) and 1(d) are characterized by a steady state without any peak, which is commonly accepted the process of dynamic recovery (DRV).

On the other hand, from Fig. 1, it can also be seen that the strain rate is a significant sensitive parameter for evaluating the trend of flow stress during plastic deformation, which reveals the work hardening tendency with an increasing strain rate. At the strain rate of 1 and 10 s^{-1}, the work hardening and recovery of the specimens reach a dynamic equilibrium, which shows a steady state flow stress. This may be due to the restriction of dislocation movement and energy accumulation under lower temperature as well as shorter time. Nevertheless, higher temperature and low strain rate provide high mobility for nucleation and growth of DRX grains.

Thus, it can be concluded that DRX is more likely to happen at lower strain rate (0.01 and 1 s^{-1}) and higher deformation temperature, whereas DRV occurs at relatively higher strain rate (1 and 10 s^{-1}), especially under lower deformation temperature.

B. Deformation constitutive equation

Generally, the relationship between flow stress and deformation conditions can be analyzed via Arrhenius equation during hot deformation. Furthermore, Zener–Hollomon parameter (Z–H parameter), which was proposed by Zener and Hollomon in 1994,[57] was a crucial hot working index and used to characterize the combined effect of temperature and strain rate on the flow stress behavior, which is expressed as follows:
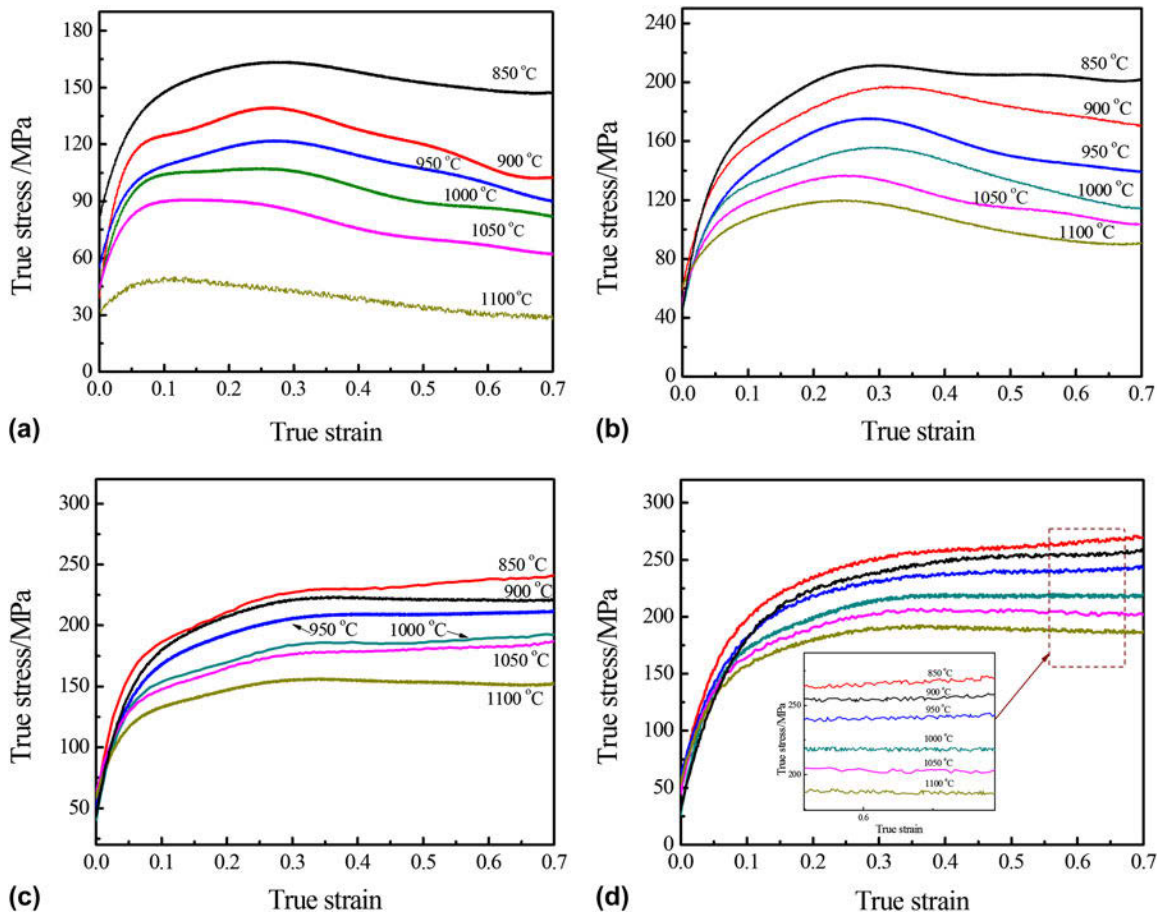

FIG. 1. True stress–true strain curves at different deformation temperatures and constant strain rate (a) $\dot{\varepsilon} = 0.01$ s^{-1}; (b) $\dot{\varepsilon} = 0.1$ s^{-1}; (c) $\dot{\varepsilon} = 1$ s^{-1}; (d) $\dot{\varepsilon} = 10$ s^{-1}.
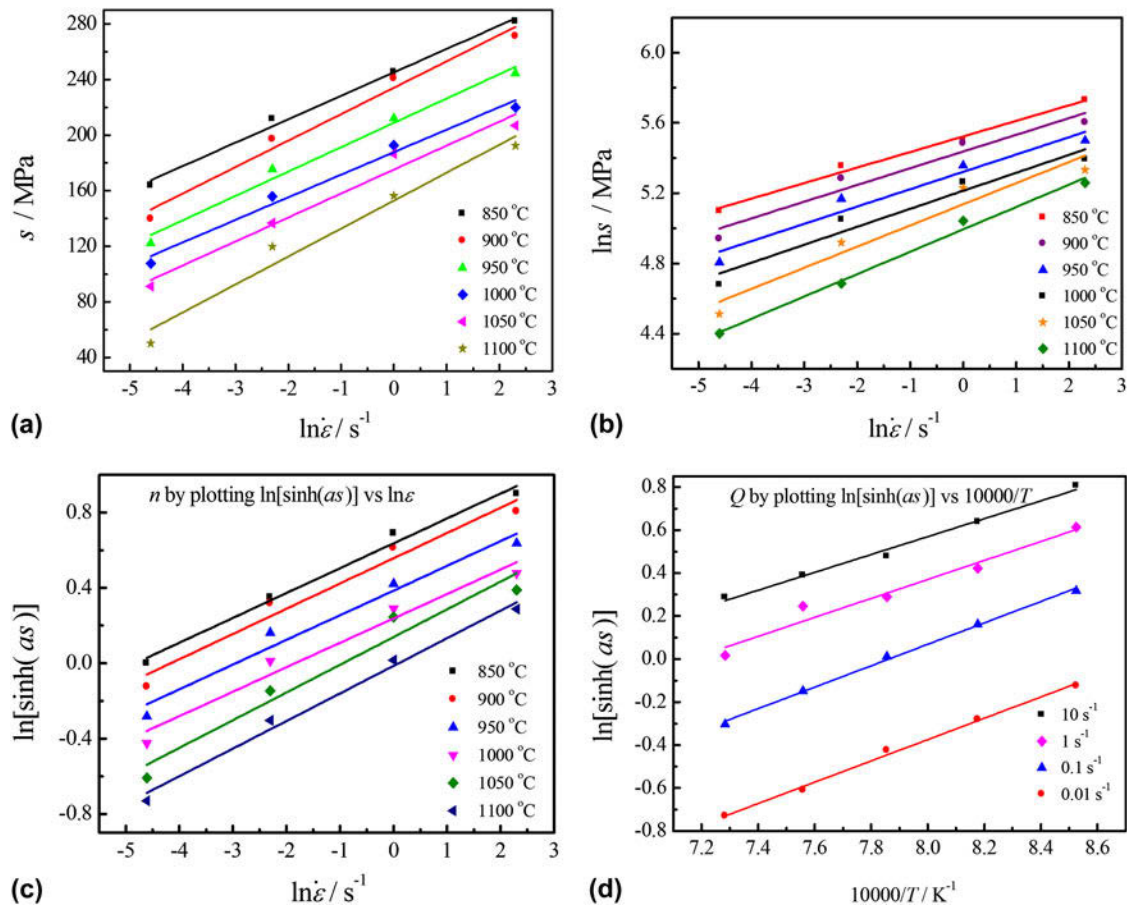
FIG. 2. Relationship between (a) σ and $\ln\dot{\varepsilon}$; (b) $\ln\sigma$ and $\ln\dot{\varepsilon}$; (c) $\ln[\sinh(\alpha\sigma)]$ and $\ln\dot{\varepsilon}$; (d) $\ln[\sinh(\alpha\sigma)]$ and $10{,}000/T$ at different deformation conditions.
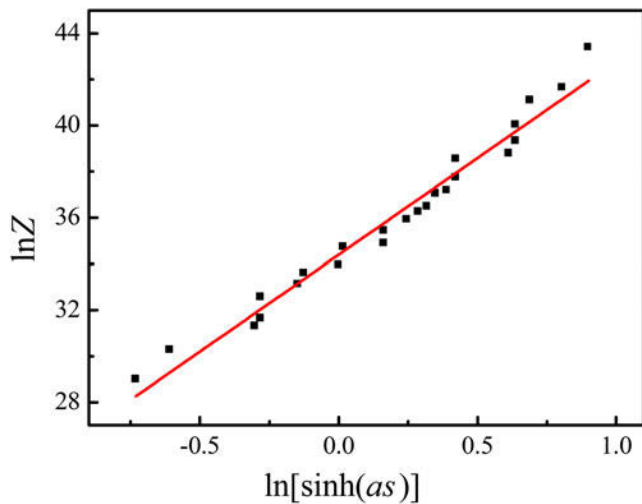

FIG. 3. Relationship between $\ln Z$ and $\ln[\sinh(\alpha\sigma)]$ for the experimental alloy.

TABLE I. Values of the material constants of Fe–36%Ni Invar alloy at different deformation strains.

True strain	β	α	n	Q (kJ/mol)	$\ln A$
0.05	0.153349	0.008207	14.17891	399.360	35.34685
0.1	0.094339	0.007103	10.04718	285.920	24.50055
0.15	0.077854	0.006662	8.86451	281.873	24.20479
0.2	0.067462	0.006084	8.86179	284.174	24.97507
0.25	0.062367	0.005939	8.08492	269.969	23.62391
0.3	0.058601	0.005916	7.60370	268.978	23.52118
0.35	0.054662	0.005991	7.16052	256.936	22.96964
0.4	0.051962	0.006150	6.42722	249.251	21.66977
0.45	0.049772	0.006313	5.97463	235.554	20.37144
0.5	0.048072	0.006406	5.67230	223.144	19.20838
0.55	0.046877	0.006495	5.44476	219.487	18.86735
0.6	0.045800	0.006569	5.251681	217.383	18.68130

$$\dot{\varepsilon} = A_1\sigma^{n_1} \cdot \exp[-Q/(RT)] \quad \alpha\sigma < 0.8 \quad , \qquad (2)$$

$$\dot{\varepsilon} = A_2 \cdot \exp(\beta\sigma) \cdot \exp[-Q/(RT)] \quad \alpha\sigma > 1.2 \quad , \qquad (3)$$

$$Z = \dot{\varepsilon} \cdot \exp[Q/(RT)] = f(\sigma) \quad , \qquad (1)$$

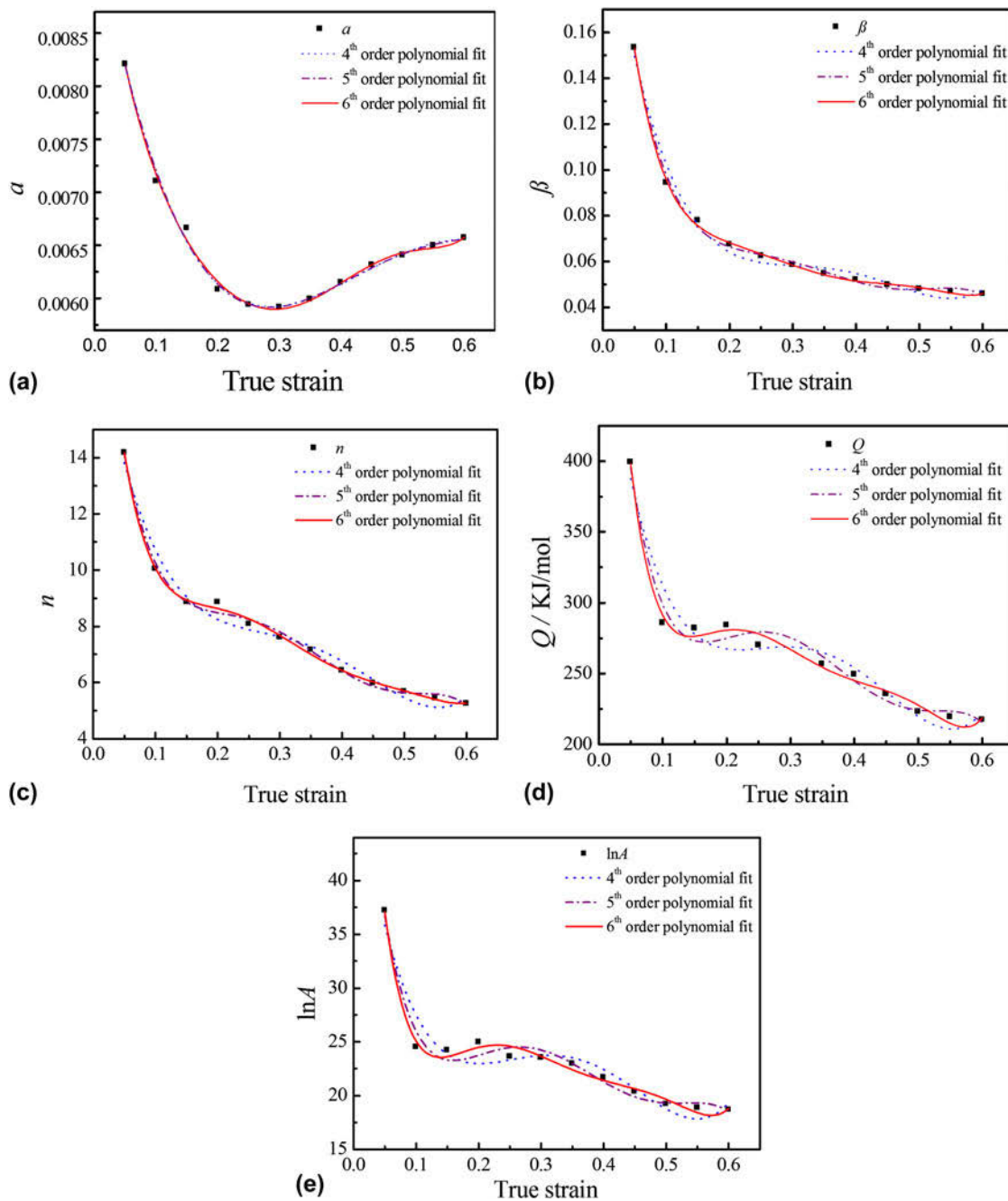$$\dot{\varepsilon} = A[\sinh(\alpha\sigma)]^n \cdot \exp[-Q/(RT)] \quad \text{for all } \sigma \quad , \qquad (4)$$

FIG. 4. Relationship between (a) α, (b) β, (c) *n*, (d) *Q*, (e) ln *A*.

where Z is the Zener–Hollomon parameter; $\dot{\varepsilon}$ is the strain rate (s^{-1}); σ is the flow stress (MPa) for a given strain; Q is the deformation activation energy (kJ/mol); R is the gas constant [8.3145 J/(mol K)]; T is the deformation temperature (K); A_1, n_1, A_2, β, A, α, and n are the material constants, $\alpha \approx \beta/n_1$. Additionally, Eq. (2) is normally used to describe the creep deformation at low-stress level. In contrast, the exponential law description of Eq. (3) is suited to illustrate higher strain rate under high-stress level, while in Eq. (4) the hyperbolic sine law can be used for all deformation conditions.

1. Determination of strain-dependent material constants

Based on the above analysis, it can be found the flow stress curves experience different deformation stages under each value of strain. Furthermore, the functional relationship between strain and the material constants can be obtained in the constitutive equations. Therefore, the compensation of strain and coefficients relative to the material should be taken into account when deriving the constitutive equation. From Eqs. (2) and (3), the

TABLE II. Coefficients of the polynomial for α, β, n, Q, and $\ln A$.

| α	β	n	Q	$\ln A$
$a_0 = 0.00998$	$b_0 = 0.29325$	$c_0 = 25.37963$	$d_0 = 746.02588$	$e_0 = 76.08817$
$a_1 = -0.04724$	$b_1 = -4.08492$	$c_1 = -335.47325$	$d_1 = -10,875.25889$	$e_1 = -1216.7817$
$a_2 = 0.28001$	$b_2 = 31.28468$	$c_2 = 2732.81246$	$d_2 = 97,579.63903$	$e_2 = 10,836.56145$
$a_3 = -1.14957$	$b_3 = -126.56914$	$c_3 = -11,298.70967$	$d_3 = -432,386.1054$	$e_3 = -47,344.54483$
$a_4 = 2.98287$	$b_4 = 277.30693$	$c_4 = 24,560.11807$	$d_4 = 1,004,500$	$e_4 = 108,431.48162$
$a_5 = -4.02328$	$b_5 = -311.02551$	$c_5 = -26,948.30984$	$d_5 = -1,177,440$	$e_5 = -125,471.09034$
$a_6 = 2.11567$	$b_6 = 139.8852$	$c_6 = 1179.69012$	$d_6 = 549,513.162$	$e_6 = 57,912.20005$
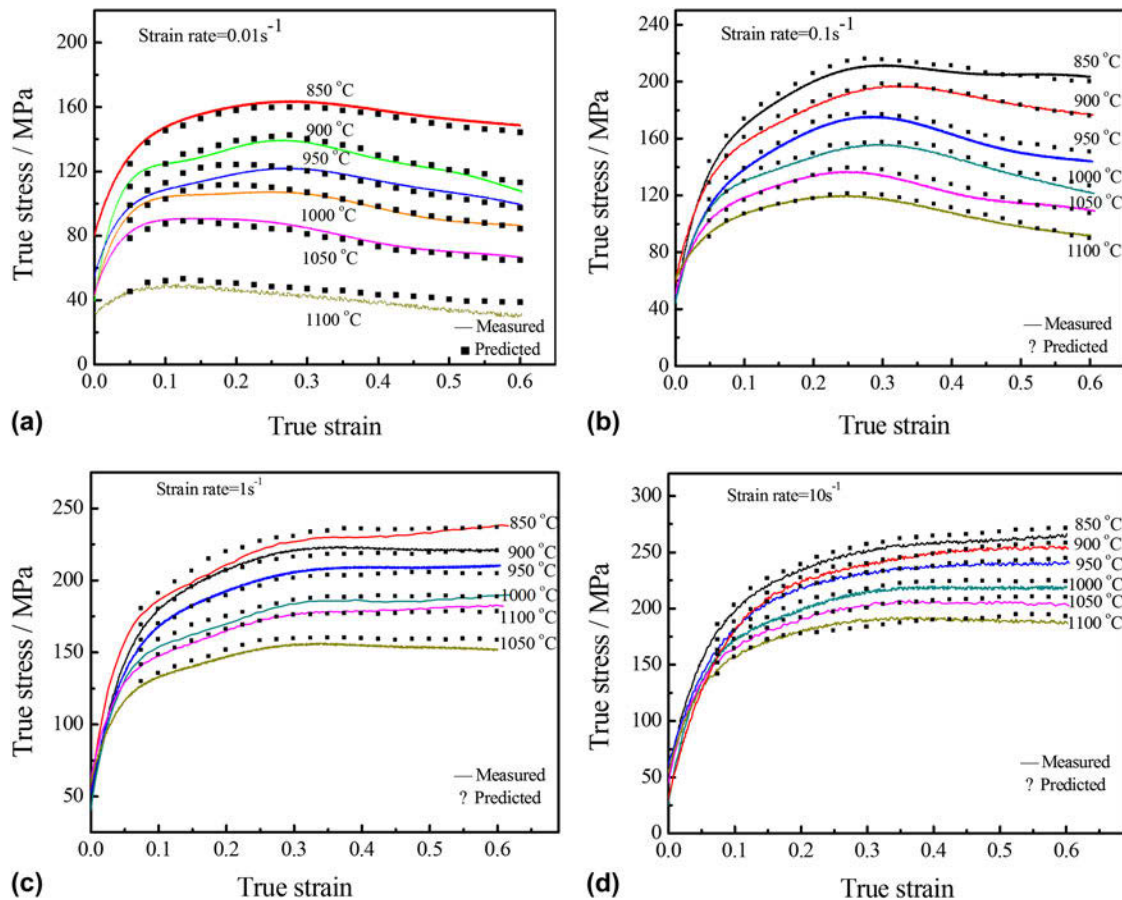
FIG. 5. Comparison between the predicted and experimental flow stress from the modified constitutive equation at the temperature of 850–1100 °C with the strain rates of (a) 0.01 s^{-1}; (b) 0.1 s^{-1}; (c) 1 s^{-1}; (d) 10 s^{-1}.

relationship between flow stress and strain rate are described as follows:

$$\dot{\varepsilon} = A\sigma^{n_1} \cdot \exp[-Q/(RT)] = B\sigma^{n_1} \quad \text{(for low stress level)} ,$$
(5)

$$\dot{\varepsilon} = A\exp(\beta\sigma) \cdot \exp[-Q/(RT)] = B'\exp(\beta\sigma)$$
$$\text{(for high stress level)} ,$$
(6)

where B and B' are coefficients relative to the material, which are dependent on the deformation temperature.

According to Eqs. (5) and (6), we can obtain

$$\ln \sigma = \frac{1}{n_1}\ln \dot{\varepsilon} - \frac{1}{n_1}\ln B ,$$
(7)

$$\sigma = \frac{1}{\beta}\ln \dot{\varepsilon} - \frac{1}{\beta}\ln B' .$$
(8)

It is noticed that the values of n_1 and β can be respectively received from the reciprocals of the slopes of the lines in $\ln \sigma - \ln \dot{\varepsilon}$ and $\sigma - \ln \dot{\varepsilon}$, as plotted in Figs. 2(a) and 2(b). Considering the slops of the lines at different temperatures is approximately same. Thus, the

mean value of n_1 and β are calculated to be 9.68611 and 0.055781 MPa^{-1} by the linear fitting method, respectively. And $\alpha = \beta/n_1 = 0.0057\ MPa^{-1}$.

Equation (4) after differentiating can be re-written as:

$$\ln[\sinh(\alpha\sigma)] = \ln\dot{\varepsilon}/n + Q/(nRT) - \ln A/n \quad . \quad (9)$$

Base on Eq. (9), Q is calculated at a given strain rate as follows:

$$Q = 10{,}000nR\frac{\partial\{\ln[\sinh(\alpha\sigma)]\}}{\partial(10{,}000/T)} \quad . \quad (10)$$

Similarly, the values of $1/n$ and Q are calculated from the slops of lines in $\ln[\sinh(\alpha\sigma)] - \ln\dot{\varepsilon}$ plot and $\ln[\sinh(\alpha\sigma)] - 1000/T$ plot [as shown in Figs. 2(c) and 2(d)], respectively. Hence, the mean values of n and Q are 5.286 and 383.64 KJ/mol. The value of $\ln A$ is determined from the interception of the same lines as Q. Then, by substituting the values of Q, $\dot{\varepsilon}$, and T into Eq. (1), the value of Z can be calculated under different deformation conditions.

According to Eqs. (1) and (4), gives:

$$Z = \dot{\varepsilon} \cdot \exp[Q/(RT)] = A[\sinh(\alpha\sigma)]^n \quad . \quad (11)$$

Taking natural logarithm on both sides of Eq. (11), we can obtain

$$\ln Z = \ln A + n\ln[\sinh(\alpha\sigma)] \quad . \quad (12)$$

According to Eq. (12), the values of $\ln A$ and n are determined by the intercept and slope of $\ln Z - \ln[\sinh(\alpha\sigma)]$ plot (as seen in Fig. 3) and the values are 34.37381, and 8.378, respectively.

2. Compensation of strain

Most importantly, the values of α, β, n, Q, and $\ln A$ were calculated at various different strains with the range of 0.05–0.6, as displayed in Table I. Then, the polynomial fit was used to illustrate the effect of deformation strain on the material constants, as presented in Fig. 4. It can be seen that although the fourth or fifth order polynomial fit can reflect the trend of the curves, the sixth order polynomial fitting was more accurate and reliable. So the sixth polynomial fitting formulas are given in Eq. (13) and the corresponding polynomial coefficients are listed in Table II.

$$\begin{cases} \alpha = a_0 + a_1\varepsilon + a_2\varepsilon^2 + a_3\varepsilon^3 + a_4\varepsilon^4 + a_5\varepsilon^5 + a_6\varepsilon^6 \\ \beta = b_0 + b_1\varepsilon + b_2\varepsilon^2 + b_3\varepsilon^3 + b_4\varepsilon^4 + b_5\varepsilon^5 + b_6\varepsilon^6 \\ n = c_0 + c_1\varepsilon + c_2\varepsilon^2 + c_3\varepsilon^3 + c_4\varepsilon^4 + c_5\varepsilon^5 + c_6\varepsilon^6 \\ Q = d_0 + d_1\varepsilon + d_2\varepsilon^2 + d_3\varepsilon^3 + d_4\varepsilon^4 + d_5\varepsilon^5 + d_6\varepsilon^6 \\ \ln A = e_0 + e_1\varepsilon + e_2\varepsilon^2 + e_3\varepsilon^3 + e_4\varepsilon^4 + e_5\varepsilon^5 + e_6\varepsilon^6 \end{cases} \quad . \quad (13)$$

Combining with Eq. (11) and the definition of the hyperbolic law, the relationship between the flow stress and the Zener–Holloman parameter can be expressed as follows:

$$\sigma = \frac{1}{\alpha}\ln\left\{\left(\frac{Z}{A}\right)^{1/n} + \left[\left(\frac{Z}{A}\right)^{2/n} + 1\right]^{1/2}\right\} \quad . \quad (14)$$

Finally, the modified constitutive equations considering the compensation of strain, which can accurately predict the flow at different strains, are given as follows:

$$\begin{cases} Z = \dot{\varepsilon} \cdot \exp[Q/(RT)] \\ \alpha = 0.00998 - 0.04724\varepsilon + 0.28001\varepsilon^2 - 1.14957\varepsilon^3 \\ \quad +2.98287\varepsilon^4 - 4.02328\varepsilon^5 + 2.11567\varepsilon^6 \\ \beta = 0.29325 - 4.08492\varepsilon + 31.28468\varepsilon^2 - 126.56914\varepsilon^3 \\ \quad +277.30693\varepsilon^4 - 311.02551\varepsilon^5 + 139.8852\varepsilon^6 \\ n = 25.37963 - 335.47325\varepsilon + 2732.81246\varepsilon^2 - 11{,}298.70967\varepsilon^3 \\ \quad +24{,}560.11807\varepsilon^4 - 26{,}948.30984\varepsilon^5 + 11{,}796.69012\varepsilon^6 \\ Q = 746.02588 - 10{,}875.25889\varepsilon + 97{,}579.63903\varepsilon^2 - 432{,}386.1054\varepsilon^3 \\ \quad +1{,}004{,}500\varepsilon^4 - 1{,}177{,}440\varepsilon^5 + 549{,}513.162\varepsilon^6 \\ \ln A = 76.08817 - 1216.7817\varepsilon + 10{,}836.56145\varepsilon^2 - 47{,}344.54483\varepsilon^3 \\ \quad +10{,}8431.48162\varepsilon^4 - 125{,}471.09034\varepsilon^5 + 57{,}912.20005\varepsilon^6 \\ \sigma = \frac{1}{\alpha}\ln\left\{\left(\frac{Z}{A}\right)^{1/n} + \left[\left(\frac{Z}{A}\right)^{2/n} + 1\right]^{1/2}\right\} \end{cases} \quad . \quad (15)$$

3. Verification of the modified constitutive equation

To confirm the accuracy of modified constitutive equation of Fe–36%Ni Invar alloy at elevated temperature, comparison between the calculated flow stress values and the experimental flow stress plots are shown in Fig. 5. It can be seen that the deviation between the calculated and measured flow stress values at strain rates from 0.01 to 10 s^{-1} as well as deformation temperatures from 850 to 1100 °C are very small. In other words, the proposed deformation constitutive equation can be used to accurately estimate the flow stress, which also provides some closely related information about the metal forming process. Thereby, the modified constitutive equation can quantify its predictability by virtue of standard statistical parameters such as correlation coefficient R and average absolute relative error AARE, which is expressed as follows:

$$R = \frac{\sum\limits_{i=1}^{N} (E_i - \bar{E})(P_i - \bar{P})}{\sqrt{\sum\limits_{i=1}^{N} (E_i - \bar{E})^2 \sum\limits_{i=1}^{N} (P_i - \bar{P})^2}} \quad , \quad (16)$$

$$\text{AARE}(\%) = \frac{1}{N} \sum\limits_{i=1}^{N} \left| \frac{E_i - P_i}{E_i} \right| \times 100 \quad , \quad (17)$$

where E is the experimental value; P is the predicted value obtained from the modified constitutive equation; $\bar{E}$ and $\bar{P}$ is the mean values of M and P, respectively. N is the total number of data points applied in the calculation. The linear relationship between the experimental and predicted flow stress values are presented in Fig. 6.
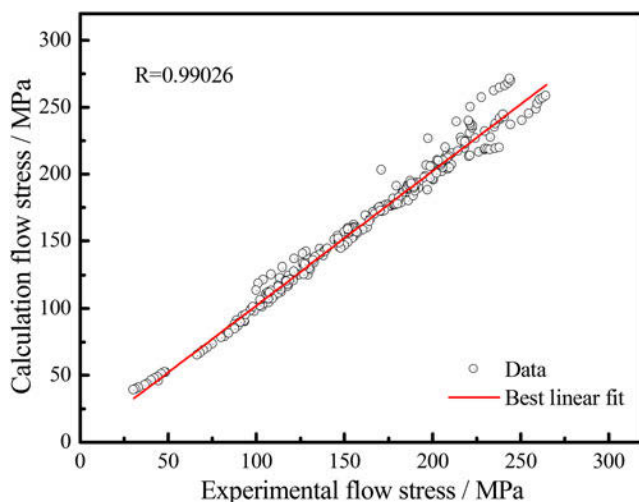
It is widely admitted that R value is used to explain the relevance of the linear fitting between the experimental and predicted data, while the AARE is computed via a term by term comparison of the relative error. Therefore, the AARE is more reliable to predict the accuracy of the modified constitutive equation. As shown in Fig. 6, the values of R and AARE are found to be 99.026% and 3.94%, respectively. In concrete terms, these statistical analyses can verify the accuracy and reliability of the modified constitutive equation at deformation conditions for the Fe–36%Ni Invar alloy.

4. Zener–Holloman parameter map

As mentioned above, the temperature and strain rate are two crucial factors to experimental materials during hot deformation. From Eq. (1), it can be seen that the effects of deformation temperature and strain rate are combined by Z–H parameter. Therefore, combined Z–H parameter and the modified constitutive equation, Z–H parameter map can be established at a given strain to exhibit the connection between temperatures and strain rates, and evaluated the extent of DRX.[21,42,43]

Figure 7 illustrates that the deformation temperatures in the range of 850–1100 °C and the strain rates of 0.01–10 s^{-1} have prominent influence on Z–H parameter. It is noted from the map that contour numbers denote the value of ln Z and shaded region represents the occurrence of DRX behavior at a strain of 0.7. Furthermore, the value of ln Z declines steadily with increase in temperature or decrease in strain rate. Most importantly, according to the Z–H parameter map, it can be concluded that the DRX behavior of deformed specimens are more likely to take place when the ln Z is <33 s^{-1} and the Z–H parameter peaks at 850 °C, 10 s^{-1}. The lower the values of ln Z the more easily DRX may occur, which means large extent of dynamic softening happened.

FIG. 6. Correlation between the experimental and calculated flow stress values obtained from the modified constitutive equation.
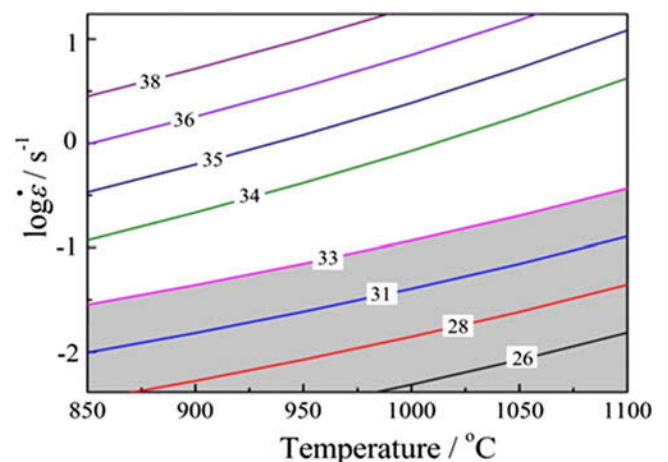

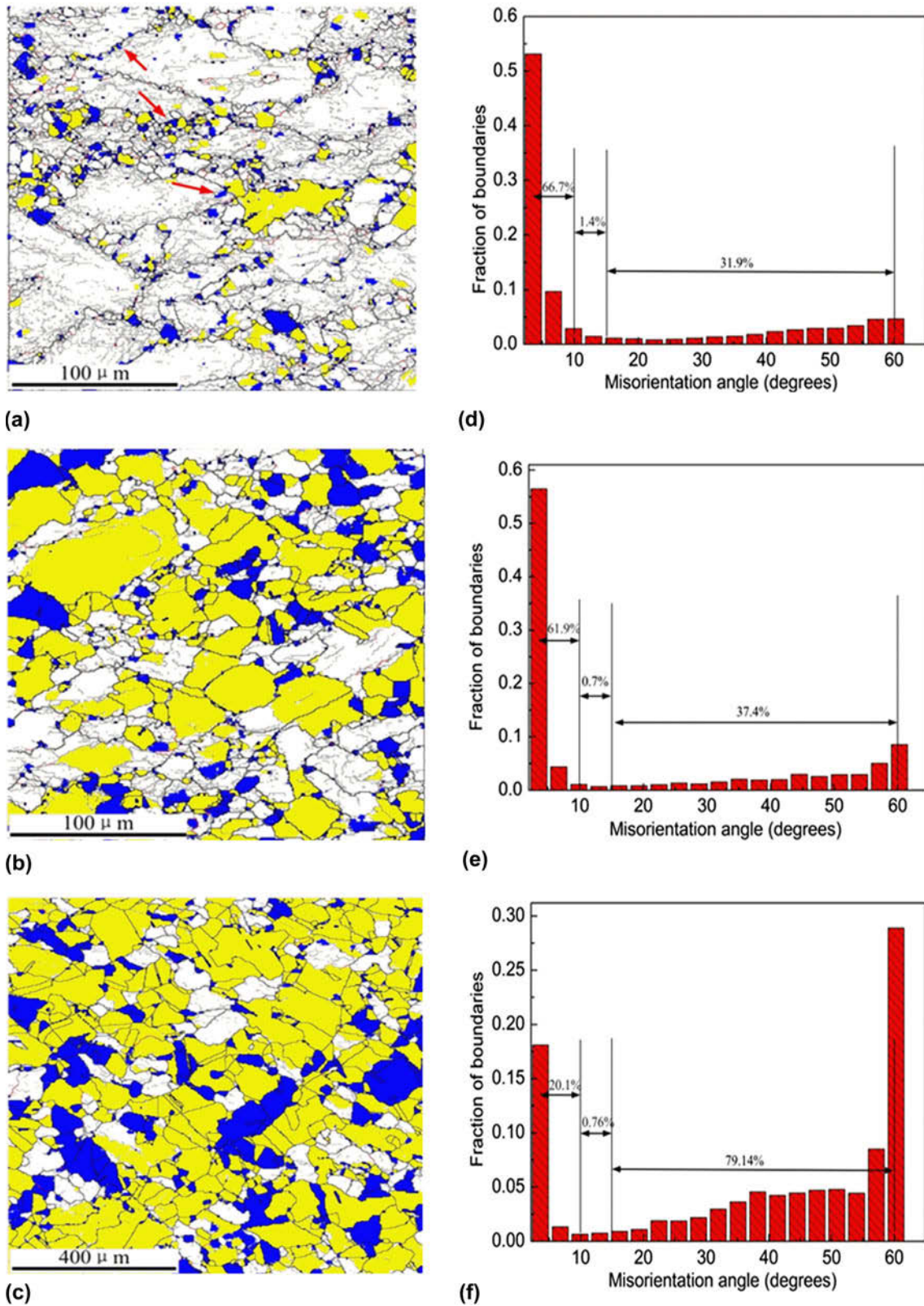FIG. 7. Z–H parameter map at the strain of 0.7. Contour numbers presents the values of ln Z.

FIG. 8. EBSD analyses the microstructures and grain boundaries misorientation angles at a strain rate of 0.01 s⁻¹ at deformed conditions of (a), (d) 850 °C, ln Z = 30.9 s⁻¹; (b), (e) 950 °C, ln Z = 28.6 s⁻¹; (c), (f) 1100 °C, ln Z = 24.3 s⁻¹. The fully recrystallized, sub-structured, and deformed grains are revealed with blue, yellow, and white colors, respectively. The low angle grain boundaries (misorientation between 2° and 10°), medium angle grain boundaries (misorientation between 10° and 15°) and high angle grain boundaries (misorientation more than 15°) are shown as gray, red, and black lines, respectively.

With the help of electron backscattered diffraction (EBSD) technique, Figs. 8(a)–8(c) further reveal the proportion of recrystallized and the sub-structured grains distinctly increased with the decrease of ln Z value and the increase of temperature. This phenomenon exhibits that the higher deformation temperature provided more energy, which was beneficial in the nucleation and growth of recrystallized grain. The red arrows in Fig. 8(a) show that new recrystallized grains occurred at the intensive area of low angle grain boundaries (LAGBs) at 850 °C. Combined with Figs. 8(d)–8(f), we find that with the value of ln Z dropped from 30.9 to 24.3, the frequency of LAGBs decreased from 66.7 to 20.1% and high angle grain boundaries (HAGBs) increased from 31.9 to 79.14%, while the medium angle grain boundaries (MAGBs) only marginally declined. It can be inferred that during this deformation process, a large fraction of LAGBs would merge and be converted into HAGBs, which was a noticeable feature of continuous DRX.[58,59] So to some extent, the analysis of microstructure evolution verified the accurate estimation of Z–H parameter map.

IV. CONCLUSION

(1) The flow stress of Fe–36%Ni Invar alloy enhanced with the increasing of strain rate and the decreasing of deformation temperature, which can be displayed by Zener–Hollomon parameter in Arrhenius type equation.

(2) The constitutive analysis illustrated that strain has significant effect on the flow stress, material constants (i.e., α, β, n, and ln A) and hot deformation activation energy (Q). Then, sixth order polynomial fit method significantly optimized the relationship between the compensation of strain and material constants, hot deformation activation energy.

(3) The modified constitutive equation can accurately and reliably predict the flow stress by the average absolute relative error (AARE was found to be 99.026%) in the hot deformation conditions.

(4) According to the Z–H parameter map, the value of ln Z declined steadily with increase in temperature or decrease in strain rate. Additionally, it can be concluded that the DRX behavior were more likely to occur when the ln Z is <33 s^{-1}.

ACKNOWLEDGMENT

REFERENCES

1. M. Lentz, S. Gall, F. Schmack, H.M. Mayer, and W. Reimers: Hot working behavior of a WE54 magnesium alloy. *J. Mater. Sci.* **49**, 1121 (2013).

2. M. Soliman and H. Palkowski: Influence of hot working parameters on microstructure evolution, tensile behavior and strain aging potential of bainitic pipeline steel. *Mater. Des.* **88**, 759 (2015).

3. C.Y. Sun, N. Guo, M.W. Fu, and C. Liu: Experimental investigation and modeling of ductile fracture behavior of TRIP780 steel in hot working conditions. *Int. J. Mech. Sci.* **110**, 108 (2016).

4. M.E. Mehtedi, F. Musharavati, and S. Spigarelli: Modelling of the flow behaviour of wrought aluminium alloys at elevated temperatures by a new constitutive equation. *Mater. Des.* **54**, 869 (2014).

5. Y.C. Lin, Q.F. Li, Y.C. Xia, and L.T. Li: A phenomenological constitutive model for high temperature flow stress prediction of Al–Cu–Mg alloy. *Mater. Sci. Eng., A* **534**, 654 (2012).

6. H.Y. Li, Y. Liu, X.C. Lu, and X.J. Su: Constitutive modeling for hot deformation behavior of ZA27 alloy. *J. Mater. Sci.* **47**, 5411 (2012).

7. X. Wang, K. Chandrashekhara, S.A. Rummel, S. Lekakh, D.C. Van Aken, and R.J. O'Malley: Modeling of mass flow behavior of hot rolled low alloy steel based on combined Johnson–Cook and Zerilli–Armstrong model. *J. Mater. Sci.* **52**, 2800 (2016).

8. D. Samantaray, S. Mandal, and A.K. Bhaduri: A comparative study on Johnson Cook, modified Zerilli–Armstrong and Arrhenius-type constitutive models to predict elevated temperature flow behaviour in modified 9Cr–1Mo steel. *Comput. Mater. Sci.* **47**, 568 (2009).

9. A. Abbasi-Bani, A. Zarei-Hanzaki, M.H. Pishbin, and N. Haghdadi: A comparative study on the capability of Johnson–Cook and Arrhenius-type constitutive equations to describe the flow behavior of Mg–6Al–1Zn alloy. *Mech. Mater.* **71**, 52 (2014).

10. Y. Sun, W.H. Ye, and L.X. Hu: Constitutive modeling of high-temperature flow behavior of Al–0.62Mg–0.73Si aluminum alloy. *J. Mater. Eng. Perform.* **25**, 1621 (2016).

11. J. Zhao, Z. Jiang, G. Zu, W. Du, X. Zhang, and L. Jiang: Flow behaviour and constitutive modelling of a ferritic stainless steel at elevated temperatures. *Met. Mater. Int.* **22**, 474 (2016).

12. Y.B. Tan, J.L. Duan, L.H. Yang, W.C. Liu, J.W. Zhang, and R.P. Liu: Hot deformation behavior of Ti–20Zr–6.5Al–4V alloy in the $\alpha + \beta$ and single β phase field. *Mater. Sci. Eng., A* **609**, 226 (2014).

13. H.R.R. Ashtiani and P. Shahsavari: Strain-dependent constitutive equations to predict high temperature flow behavior of AA2030 aluminum alloy. *Mech. Mater.* **100**, 209 (2016).

14. M. Zhou, Y.C. Lin, J. Deng, and Y.Q. Jiang: Hot tensile deformation behaviors and constitutive model of an Al–Zn–Mg–Cu alloy. *Mater. Des.* **59**, 141 (2014).

15. C. Zhang, J. Ding, Y. Dong, G. Zhao, A. Gao, and L. Wang: Identification of friction coefficients and strain-compensated Arrhenius-type constitutive model by a two-stage inverse analysis technique. *Int. J. Mech. Sci.* **98**, 195 (2015).

16. P. Changizian, A. Zarei-Hanzaki, and A.A. Roostaei: The high temperature flow behavior modeling of AZ81 magnesium alloy considering strain effects. *Mater. Des.* **39**, 384 (2012).

17. D.H. Yu: Modeling high-temperature tensile deformation behavior of AZ31B magnesium alloy considering strain effects. *Mater. Des.* **51**, 323 (2013).

18. S.A. Askariani and S.M. Hasan Pishbin: Hot deformation behavior of Mg–4Li–1Al alloy via hot compression tests. *J. Alloys Compd.* **688**, 1058 (2016).

19. F. Gao, Z. Liu, R.D.K. Misra, H. Liu, and F. Yu: Constitutive modeling and dynamic softening mechanism during hot deformation of an ultra-pure 17%Cr ferritic stainless steel stabilized with Nb. *Met. Mater. Int.* **20**, 939 (2014).

20. Y. Cao, H. Di, R.D.K. Misra, X. Yi, J. Zhang, and T. Ma: On the hot deformation behavior of AISI 420 stainless steel based on constitutive analysis and CSL model. *Mater. Sci. Eng., A* **593**, 111 (2014).

21. A. Marandi, A. Zarei-Hanzaki, N. Haghdadi, and M. Eskandari: The prediction of hot deformation behavior in Fe–21Mn–2.5Si–1.5Al transformation-twinning induced plasticity steel. *Mater. Sci. Eng., A* **554**, 72 (2012).

22. S.W. Wu, X.G. Zhou, G.M. Cao, Z.Y. Liu, and G.D. Wang: The improvement on constitutive modeling of Nb–Ti micro alloyed steel by using intelligent algorithms. *Mater. Des.* **116**, 676 (2017).

23. L. Wang, F. Liu, J.J. Cheng, Q. Zuo, and C.F. Chen: Arrhenius-type constitutive model for high temperature flow stress in a Nickel-based corrosion-resistant alloy. *J. Mater. Eng. Perform.* **25**, 1394 (2016).

24. D. Samantaray, A. Patel, U. Borah, S.K. Albert, and A.K. Bhaduri: Constitutive flow behavior of IFAC-1 austenitic stainless steel depicting strain saturation over a wide range of strain rates and temperatures. *Mater. Des.* **56**, 565 (2014).

25. J. Cai, Y. Lei, K. Wang, X. Zhang, C. Miao, and W. Li: A comparative investigation on the capability of modified Zerilli–Armstrong and Arrhenius-type constitutive models to describe flow behavior of BFe10-1-2 cupronickel alloy at elevated temperature. *J. Mater. Eng. Perform.* **25**, 1952 (2016).

26. Z. Guan, M. Ren, P. Zhao, P. Ma, and Q. Wang: Constitutive equations with varying parameters for superplastic flow behavior of Al–Zn–Mg–Zr alloy. *Mater. Des.* **54**, 906 (2014).

27. W. Jia, S. Xu, Q. Le, L. Fu, L. Ma, and Y. Tang: Modified Fields–Backofen model for constitutive behavior of as-cast AZ31B magnesium alloy during hot deformation. *Mater. Des.* **106**, 120 (2016).

28. L.C. Tsao, Y.T. Huang, and K.H. Fan: Flow stress behavior of AZ61 magnesium alloy during hot compression deformation. *Mater. Des.* **53**, 865 (2014).

29. Y. Zhu, W. Zeng, Y. Sun, F. Feng, and Y. Zhou: Artificial neural network approach to predict the flow stress in the isothermal compression of as-cast TC21 titanium alloy. *Comput. Mater. Sci.* **50**, 1785 (2011).

30. Y. Han, W. Zeng, Y. Zhao, Y. Qi, and Y. Sun: An ANFIS model for the prediction of flow stress of Ti600 alloy during hot deformation process. *Comput. Mater. Sci.* **50**, 2273 (2011).

31. Y.J. Qin, Q.L. Pan, Y.B. He, W.B. Li, X.Y. Liu, and X. Fan: Artificial neural network modeling to evaluate and predict the deformation behavior of ZK60 magnesium alloy during hot compression. *Mater. Manuf. Processes* **25**, 539 (2010).

32. O. Sabokpa, A. Zarei-Hanzaki, H.R. Abedi, and N. Haghdadi: Artificial neural network modeling to predict the high temperature flow behavior of an AZ81 magnesium alloy. *Mater. Des.* **39**, 390 (2012).

33. G.Z. Quan, T. Wang, Y.L. Li, Z.Y. Zhan, and Y.F. Xia: Artificial neural network modeling to evaluate the dynamic flow stress of 7050 aluminum alloy. *J. Mater. Eng. Perform.* **25**, 553 (2016).

34. M.H. Wang, G.T. Wang, and R. Wang: Flow stress behavior and constitutive modeling of 20MnNiMo low carbon alloy. *J. Cent. South Univ.* **23**, 1863 (2016).

35. G. Ji, G. Yang, L. Li, and Q. Li: Modeling constitutive relationship of Cu–0.4Mg alloy during hot deformation. *J. Mater. Eng. Perform.* **23**, 1770 (2014).

36. W. Peng, W. Zeng, Q. Wang, Q. Zhao, and H. Yu: Effect of processing parameters on hot deformation behavior and microstructural evolution during hot compression of as-cast Ti60 titanium alloy. *Mater. Sci. Eng., A* **593**, 16 (2014).

37. D. Samantaray, S. Mandal, C. Phaniraj, and A.K. Bhaduri: Flow behavior and microstructural evolution during hot deformation of AISI type 316 L(N) austenitic stainless steel. *Mater. Sci. Eng., A* **528**, 8565 (2011).

38. L. Guo, X. Fan, G. Yu, and H. Yang: Microstructure control techniques in primary hot working of titanium alloy bars: A review. *Chin. J. Aeronaut.* **29**, 30 (2016).

39. M.H. Wang, W.H. Wang, J. Zhou, X.G. Dong, and Y.J. Jia: Strain effects on microstructure behavior of 7050-H112 aluminum alloy during hot compression. *J. Mater. Sci.* **47**, 3131 (2011).

40. B. Wu, M.Q. Li, and D.W. Ma: The flow behavior and constitutive equations in isothermal compression of 7050 aluminum alloy. *Mater. Sci. Eng., A* **542**, 79 (2012).

41. Y. Liu, Z. Yao, Y. Ning, Y. Nan, H. Guo, C. Qin, and Z. Shi: The flow behavior and constitutive equation in isothermal compression of FGH4096–GH4133B dual alloy. *Mater. Des.* **63**, 829 (2014).

42. D. Feng, X.M. Zhang, S.D. Liu, and Y.L. Deng: Constitutive equation and hot deformation behavior of homogenized Al–7.68Zn–2.12Mg–1.98Cu–0.12Zr alloy during compression at elevated temperature. *Mater. Sci. Eng., A* **608**, 63 (2014).

43. R. Bobbili and V. Madhu: Dynamic recrystallization behavior of a biomedical Ti–13Nb–13Zr alloy. *J. Mech. Behav. Biomed. Mater.* **59**, 146 (2016).

44. X.M. Chen, Y.C. Lin, D.X. Wen, J.L. Zhang, and M. He: Dynamic recrystallization behavior of a typical nickel-based superalloy during hot deformation. *Mater. Des.* **57**, 568 (2014).

45. X. Kai, C. Chen, X. Sun, C. Wang, and Y. Zhao: Hot deformation behavior and optimization of processing parameters of a typical high-strength Al–Mg–Si alloy. *Mater. Des.* **90**, 1151 (2016).

46. H. Mirzadeh, J.M. Cabrera, A. Najafizadeh, and P.R. Calvillo: EBSD study of a hot deformed austenitic stainless steel. *Mater. Sci. Eng., A* **538**, 236 (2012).

47. N. Haghdadi, D. Martin, and P. Hodgson: Physically-based constitutive modelling of hot deformation behavior in a LDX 2101 duplex stainless steel. *Mater. Des.* **106**, 420 (2016).

48. S. Gall, M. Huppmann, H.M. Mayer, S. Müller, and W. Reimers: Hot working behavior of AZ31 and ME21 magnesium alloys. *J. Mater. Sci.* **48**, 473 (2012).

49. Y. Cao, H. Di, J. Zhang, J. Zhang, T. Ma, and R.D.K. Misra: An electron backscattered diffraction study on the dynamic recrystallization behavior of a nickel–chromium alloy (800H) during hot deformation. *Mater. Sci. Eng., A* **585**, 71 (2013).

50. M. Shiga: Invar alloys. *Crit. Rev. Solid State Mater. Sci.* **1**, 340 (1996).

51. W.S. Park, M.S. Chun, M.S. Han, M.H. Kim, and J.M. Lee: Comparative study on mechanical behavior of low temperature application materials for ships and offshore structures: Part I—Experimental investigations. *Mater. Sci. Eng., A* **528**, 5790 (2011).

52. W. Xiong, H. Zhang, L. Vitos, and M. Selleby: Magnetic phase diagram of the Fe–Ni system. *Acta Mater.* **59**, 521 (2011).

53. Y. He, F. Wang, C. Li, Z. Yang, J. Zhang, and Y. Li: Effect of Mg content on the hot ductility of wrought Fe–36Ni alloy with Ti addition. *Mater. Sci. Eng., A* **673**, 99 (2016).

54. J.L. Valenzuela, J.F. Valderruten, G.A. Pérez Alcázar, H.D. Colorado, J.J. Romero, J.M. González, J.M. Greneche, and J.F. Marco: Low temperature study of mechanically alloyed $Fe_{67.5}Ni_{32.5}$ Invar sample. *J. Magn. Magn. Mater.* **385**, 83 (2015).

55. T. Michler: Influence of gaseous hydrogen on the tensile properties of Fe–36Ni Invar alloy. *Int. J. Hydrogen Energy* **39**, 11807 (2014).

56. J.J. Zheng, C.S. Li, S. He, B. Cai, and Y.L. Song: Microstructural and tensile behavior of Fe–36%Ni alloy after cryorolling and subsequent annealing. *Mater. Sci. Eng., A* **670**, 275 (2016).

57. C. Zener and J.H. Hollomon: Effect of strain rate upon plastic flow of steel. *J. Appl. Phys.* **15**, 22 (1944).

58. X.Q. Yin, C.H. Park, Y.F. Li, W.J. Ye, Y.T. Zuo, S.W. Lee, J.T. Yeom, and X.J. Mi: Mechanism of continuous dynamic recrystallization in a 50Ti–47Ni–3Fe shape memory alloy during hot compressive deformation. *J. Alloys Compd.* **693**, 426 (2017).

59. T. Sakai, A. Belyakov, R. Kaibyshev, H. Miura, and J.J. Jonas: Dynamic and post-dynamic recrystallization under hot, cold and severe plastic deformation conditions. *Prog. Mater. Sci.* **60**, 130 (2014).